Chapter 5

Synthesis and Characterization of Noble Metal-Free Nanoparticles for Enhanced Oxygen Reduction Electrocatalysis

Outline

There is an increasing demand for clean substitutes of traditional fossil fuel; the fuel cell [1] metal-air batteries [2], supercapacitors [3], lithium-ion batteries [4], etc. has created various scientific and technological importances over the last decade. The cathodic ORR is an essential process in the functioning of PEMFCs. The sluggish kinetic behaviour of ORR is the major limiting factor for their worldwide commercialization and utilization of the FCs [5]. Till now, Pt and its alloy based electrode materials have been the most active electrocatalysts existing in real system for improving the sluggish kinetics of ORR, however due to high cost, scarcity and poor durability of Pt [6], the PEMFCs could not ensure the place for the futuristic energy alternative in the global energy market. Till now, splendid research efforts conducted on the discovery of cost-effective alternatives to Pt-based metals. Subsequently, researcher devoted their keen attention to the design of various non-precious earth-abundant metal-based electrodes as they revealed ORR activity and stability analogous to or even superior to Pt- based electrode in the alkaline electrolyte. Among the non-precious catalysts, 1^{st} row transition metal [7], chalcogenides [8], oxynitrides [9] metal oxides [10] are promising materials used for catalyzing the crucial reaction. Yan et al. demonstrated a facile impregnation method to prepare FeCo NP decorated on defective graphene (DG). They found an extraordinary performance of ORR and free from methanol tolerance due to the unique carbon defects present in the G [7]. Among the various first-row transition metal oxide, with mixed valence spinel oxide shows superior electrocatalytic ORR activity [10,11]. Kashyap et al. synthesized spinel cobalt ferrite (CF) on nitrogen-doped reduced graphene oxide (N-rGO) by carefully adjusting the water to ethanol ratio. They have also used Vulcan carbon as an additive. The enhancement in the ORR activity has been explained based on a healthy synergistic interaction between the active site bearing N-rGO sheets and the micropores contributing by Vulcan carbon [12]. Sun and co-workers reported that spinel $CuCo_2O_4$ NPs integrated onto N-rGO through a two-step solvothermal method. The $CuCo_2O_4$/N-rGO hybrid outperform activity retention than the commercial Pt/C catalyst due to the strong coupling between these two components [13] Singh at el. reported electrochemical ORR activity of CoMn alloy oxide supported over N-doped porous graphene [14]. Again Zhao et al. prepared composites of nano-sized

delafossite $CuFeO_2$ and nitrogen-free carbon nanotubes ($CuFeO_2$–CNT-X) by a facile one-pot hydrothermal approach. The efficiency ORR activity of the catalyst was reported to be due to the synergistic effect between the nano-sized $CuFeO_2$ and CNTs which helped in the performance of the mass transport and electron transfer in nitrogen-free $CuFeO_2$–CNT-75 [15]. Wang et al. synthesized core-shell Cu/γ-Fe_2O_3@C and yolk–shell-structured Cu/Fe@γ-Fe_2O_3@C particles are prepared by pyrolysis of different precursor materials. They claimed that the metal-containing samples showed very superior ORR activity as compared with metal-free counterparts [16]. Inspiring from the above discussion, we developed two types noble metal free NPs for the enhanced fuel cell ORR in alkaline media.

This chapter is divided into two sections,

Section 5A Synthesis and Characterization of Cu-$CuFe_2O_4$/C Nanoparticles for Enhanced Oxygen Reduction Electrocatalysis

Section 5B Synthesis and Characterization CuCo/CuO-Co_3O_4/C Nanoparticles and Their Electrochemical Oxygen Reduction Reaction Activity

Section 5A: Synthesis and Characterization Cu-$CuFe_2O_4$/C Nanoparticles for Enhanced Oxygen Reduction Electrocatalysis

In this section of chapter 5 we have synthesised Cu-$CuFe_2O_4$ onto hetero-atom free Vulcan carbon through a one-step solvothermal approach at 120 ^oC. In this approach we used inexpensive $CuCl_2 \cdot 2H_2O$, $FeCl_2 \cdot 4H_2O$ as metal precursors and hydrazine hydrate as reducing agent. The as-synthesised catalysts showed very good activity towards ORR in alkaline media.

5A.1 Results and Discussion

5A.1.1 Characterization of the Synthesized Cu-$CuFe_2O_4$/C NPs

The XRD technique is used to analyze the crystallographic structure and composition of the as-fabricated Cu-$CuFe_2O_4$/C hybrid. As shown in Figure 5A.1a, we can confirm the presence of metallic Cu in the composites and all the peaks at 2θ = 43.3°, 50.4° and 74.1° are indexed to the (111), (200) and (220) reflections of the fcc phase of copper (JCPDS No. 01-085-1326) respectively [17]. The other diffraction peaks at 2θ = 18.5°, 30.2°, 35.5°, 37.2°, 43.2°, 57.1°, 62.7° and 74.2° can be ascribed to the (111), (220), (311), (222), (400), (511), (440) and (533) reflections of spinel $CuFe_2O_4$ (JCPDS No. 25-0283) [4]. Likewise, Cu-$CuFe_2O_4$ and Cu-$CuFe_2O_4$/C show the similar lattice parameter values of a = b = c = 0.8349 nm with the cubic system of the fcc lattice. A broad diffraction peak appearing at 2θ = ∼25° corresponds to the (002) reflection of a hexagonal structure in Vulcan XC-72R. Clearly, we can perceive that the Cu-$CuFe_2O_4$ samples reveal the co-occurrence of $CuFe_2O_4$ and Cu(0) (Figure 5A.1a,), signifying that with and without C-coated Cu/$CuFe_2O_4$ composite was successfully prepared by a facile one-step solvothermal method. The solvothermal experiment was carried out with a targeted metal/metal oxide loading of 20% on the carbon matrix. The TGA profile recorded under an air atmosphere (Figure 5A.1b) shows prominent weight loss region begins at 430 °C, which is attributed to the burning of carbon. The oxidation of the carbon completes at around 625 °C, leaving a residue content of ∼21% corresponding to the amount of metal/metal oxide NPs accommodated on the carbon matrix. The specific surface area of as-prepared Cu-$CuFe_2O_4$/C was analyzed by N_2 adsorption-desorption isotherm and calculated by the

Brunauer-Emmett-Teller (BET) method, as shown in (Figure 5A.1c). The BET surface area of Cu-$CuFe_2O_4$/C is 82.3 m^2 g^{-1}. The observed type-IV hysteresis (Figure 5A.1d) indicates the mesoporous nature of the materials.

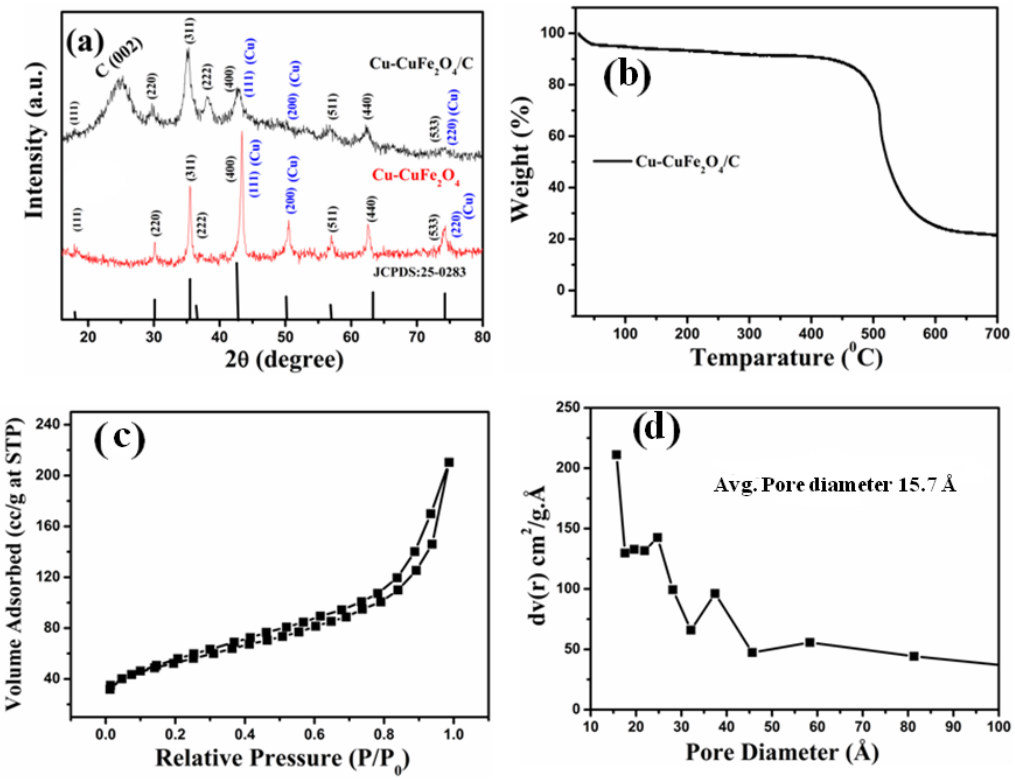

Figure 5A.1: XRD patterns (a) Cu-$CuFe_2O_4$/C (black line) and bare Cu-$CuFe_2O_4$ (red line) (b) TGA Curve (c) N_2 adsorption-desorption isotherm of Cu-$CuFe_2O_4$/C (d) Pore size distribution curve of Cu-$CuFe_2O_4$/C.

To further explore the ionization state and chemical composition of Cu-$CuFe_2O_4$/C and Cu-$CuFe_2O_4$ composites, XPS measurement was performed. Figure 5A.2a presents the survey scan of the Cu-$CuFe_2O_4$/C composites in the region of 0-1000 eV and all the indexed peaks are corresponding to Cu, Fe, C, and O. The deconvoluted high-resolution Cu XPS spectrum of Cu-$CuFe_2O_4$/C confirmed the co-existence of metallic Cu and copper oxide in the composites as shown in Figure 5A.2b. The peaks of Cu 2p spectra at around 932.8 and 952.9 eV correspond to Cu^0 $2p_{3/2}$ and $2p_{1/2}$ peaks and peaks at 934.4 and 954.3 eV due to Cu^{2+} $2p_{3/2}$ and Cu^{2+} $2p_{1/2}$, respectively. This reveals that the ionization state of Cu at the surface of the Cu-

$CuFe_2O_4$/C composites are a mixture of ionization states of 0 and +2 with the percentage of 51.1% and 48.90%, respectively [17,18]. The XPS of bare Cu-$CuFe_2O_4$ NPs also reveals the co-existence of both the form of copper, but in this case metallic form has less percentage 28.1% than that of the Cu-$CuFe_2O_4$/C nanohybrid. This may due to the easy oxidation ability of the bare NPs as shown in Figure 5A.3.

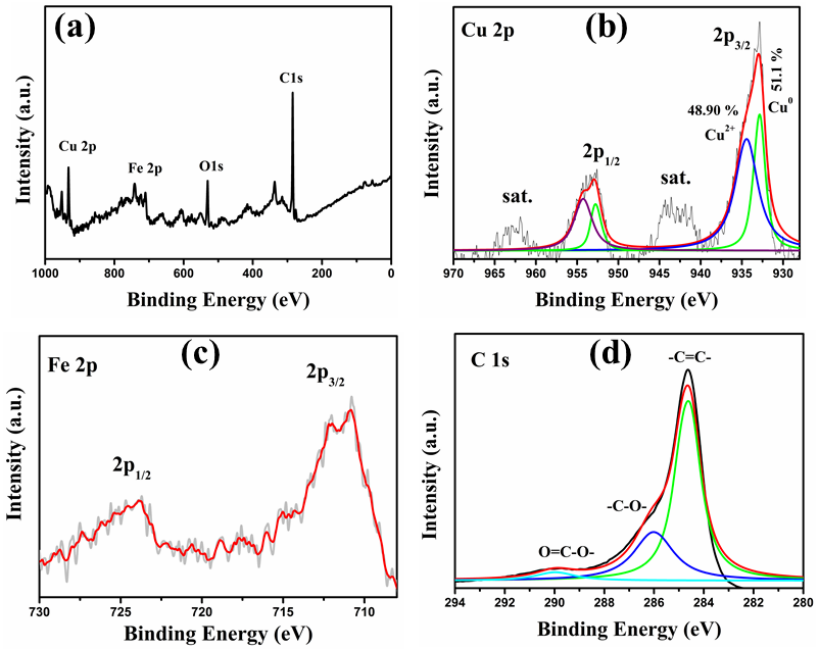

Figure 5A.2: (a) XPS survey spectrum of Cu-$CuFe_2O_4$/C. High-resolution XP spectra of (b) Cu 2p, (c) Fe 2p, (d) C 1 s for Cu-$CuFe_2O_4$/C.

As presented in Figure 5A.2c, the Fe 2p XP spectrum exhibits two peaks at 710.8 and 724.8 eV with an energy difference of 14.0 eV, are assigned to Fe^{3+} $2p_{3/2}$ and Fe^{3+} $2p_{1/2}$ spin-orbit states of Cu-$CuFe_2O_4$/C, respectively [17], The C 1s core-level XP spectrum (Figure 5A.2d) of Cu-$CuFe_2O_4$/C is slightly asymmetric and deconvoluted into different peaks, one strong peak at 284.6 eV along with two small peaks at 286 and 289.9 eV, consistent to –C=C–, −C−O−, and O=C−O− bonds, respectively. The high integration areas of −C=C− compared to the −C−O− and O=C−O− peaks specify that the O content is low [19]. The remarkable loss of oxygen-containing functional groups is ascribed to the addition of a reductive agent in the solvothermal reaction. Moreover, the positive shift of ~0.54 eV for Cu $2p_{3/2}$ and ~0.20

eV for Fe $2p_{3/2}$ observed for Cu-$CuFe_2O_4$/C as compared to that of bare Cu-$CuFe_2O_4$ signifies that strong coupling between CuFe and carbon.

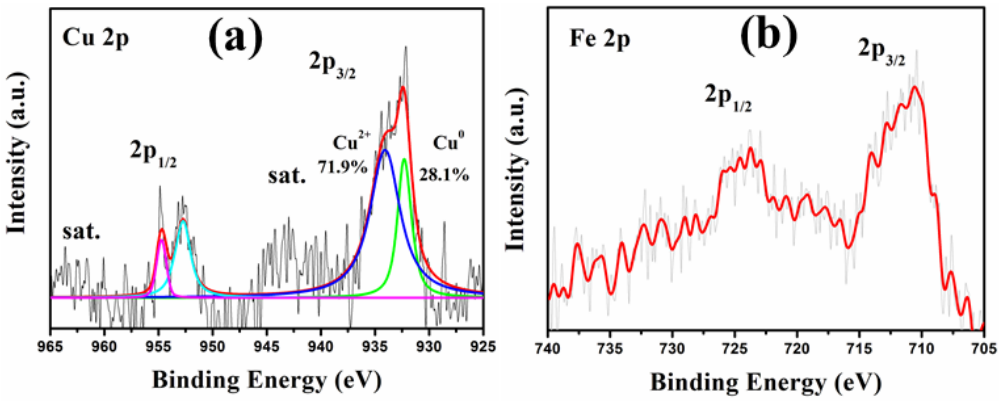

Figure 5A.3: High-resolution XPS spectra of (a) Cu 2p, (b) Fe 2p, for Cu-$CuFe_2O_4$.

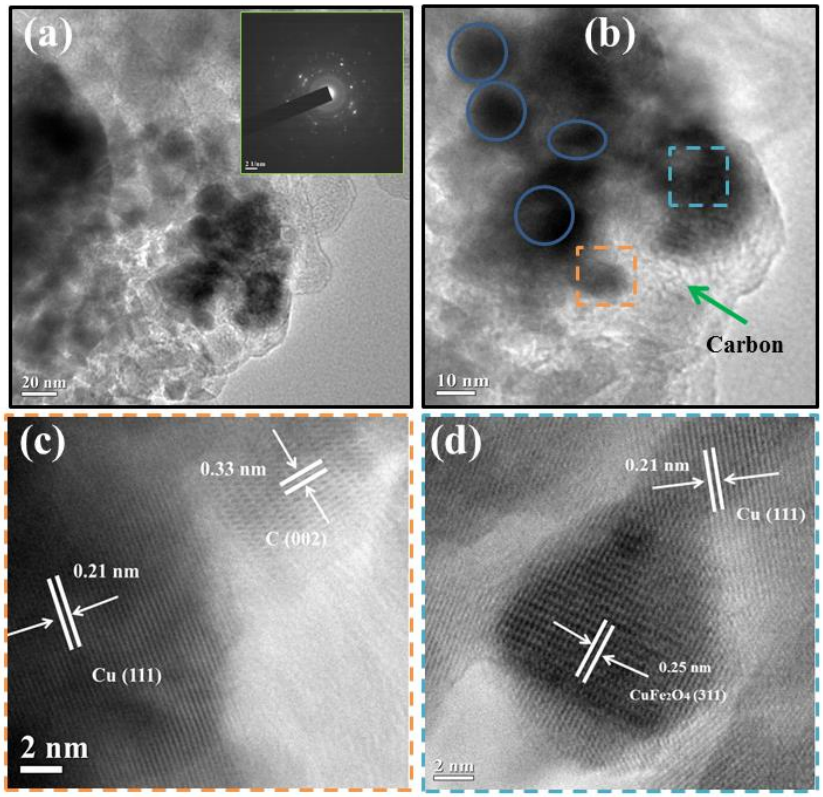

Figure 5A.4: (a) TEM images of Cu-$CuFe_2O_4$/C, inset of (a) shows the SAED pattern, (b) HRTEM image of Cu-$CuFe_2O_4$/C showing black contrast of metal/metal oxide and carbon, (c,d) HRTEM image of Cu-$CuFe_2O_4$/C with lattice fringes corresponding to various constituents.

TEM technique was used to examine the morphology and structure of Cu-$CuFe_2O_4$/C. From Figure 5A.4a it can be seen that the as-prepared Cu-$CuFe_2O_4$ has large crystal size with irregular spherical in nature. The Figure 5A.4c,d shows typical High resolution TEM images of Cu-$CuFe_2O_4$/C. It profoundly reveals the carbon matrix has a mass of fine NPs evenly embedded on them. Apparently, there are no large aggregations of Cu and $CuFe_2O_4$ in the carbon matrix, demonstrating a thriving distribution and lesser size in comparison with bare Cu-$CuFe_2O_4$ (Figure 5A.5). The synergistic effects of carbon matrix and NPs credited to the vast transformation of morphology between the two samples, in the solvothermal reaction, carbon matrix can prevent the agglomeration during the particle growth process and control the crystal nucleation and growth of Cu and $CuFe_2O_4$ [20]. Moreover, the TEM images further confirm that NPs with the diameter of 10–15 nm are decorated over carbon matrix as shown in Figure 5A.4b. The SAED pattern in the inset of Figure 5A.4a shows that several bright spots were forming diffraction rings, which confirm the polycrystalline nature of Cu-$CuFe_2O_4$/C composites. The HRTEM images (Figure 5A.4c,d) further confirm the formation of Cu-$CuFe_2O_4$/C. The interplanar spacing of 0.21 nm and 0.33 nm in Figure 5A.4c can be assigned to the (111) plan of Cu and (002) plan of carbon. The lattice fringes of 0.25 nm in Figure 5A.4d can be ascribed to the (311) plane of $CuFe_2O_4$ [5]. The distribution of Cu and $CuFe_2O_4$ is obliging for fast ion entree, stable crystalline structure, and efficient electrolyte penetration. Additionally, the hybrid system can promote the electrochemical activities, which can result in high ORR performance.

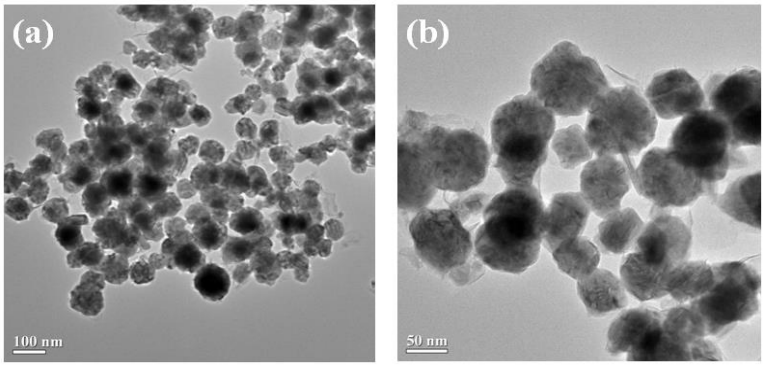

Figure 5A.5: (a) TEM images of Cu-$CuFe_2O_4$, (b) High magnitude TEM image of Cu-$CuFe_2O_4$.

5A.1.2 Electrocatalytic Activity of Cu-$CuFe_2O_4$/C NPs

CV measurements were performed to evaluate ORR performance of all the NPs. Figure 5A.6a shows the CVs of the Cu-$CuFe_2O_4$/C and other electrocatalysts in N_2- (dashed line) and O_2- (solid line) saturated 0.1 M KOH solution. A well-defined cathodic peak in the O_2-saturated solution at −0.177 V with a current density of −1.49 mA cm^{-2} was observed for the Cu-$CuFe_2O_4$/C NPs. The CVs of all electrocatalysts exhibit the characteristics ORR peak with some obvious variations on the onset potentials. However, the ORR peak of Cu-$CuFe_2O_4$/C is sharper and prominent in comparison to others. The ORR onset potential of the Cu-$CuFe_2O_4$/C NPs was ~10 V and ~12 V more positive than Cu-$CuFe_2O_4$ + C (physical mixture of Cu-$CuFe_2O_4$ and carbon) and bare Cu-$CuFe_2O_4$, respectively. Hence Cu-$CuFe_2O_4$/C shows enriched ORR activity over that of Cu-$CuFe_2O_4$ + C and bare Cu-$CuFe_2O_4$. This can be attributed to the strong electronic coupling between the carbon matrix and NPs and consequently enriches the ORR activity [21,22]. From the current density and onset potential for ORR, we can infer that bare Cu-$CuFe_2O_4$ NPs and carbon alone show inferior ORR activity. However, Cu-$CuFe_2O_4$ + C shows better ORR property compared to the individual components which further enriched in the case of Cu-$CuFe_2O_4$/C. Such ORR behaviour is also observed over Co_3O_4/N-rGO and $CuCo_2O_4$/N-rGO. [13,23]. RDE measurements were performed to quantify the ORR activity of all the catalysts. LSVs were recorded for all the catalysts, keeping the rotation rate of the working electrode at 1600 rpm in O_2-saturated 0.1 M KOH solution as presented in Figure 5A.6b. From the LSV curves the distinct variation in terms of the onset potential, half-wave potential and limiting current density of various samples are observed. The onset potential of the systems toward ORR follows the order Cu-$CuFe_2O_4$/C (−0.139 V) > Cu-$CuFe_2O_4$ + C (−0.175 V) > Cu-$CuFe_2O_4$ (−0.186 V) > Carbon (−0.218 V). A close look at the LSV data clearly indicates that Cu-$CuFe_2O_4$/C NPs tender superior ORR performance in terms of the onset potential, half-wave potential and limiting current density among all the electrocatalysts. The onset potential and half-wave potential of Cu-$CuFe_2O_4$/C are −0.139 and −0.39 V (*vs.* Ag/AgCl), respectively are 0.036 and 0.06 V higher compared to Cu-$CuFe_2O_4$ + C and 0.020 and 0.047 V than bare Cu-$CuFe_2O_4$. Additionally Cu-$CuFe_2O_4$/C NPs shows a

considerable improvement in the limiting current density due to the chemical association of carbon in the hybrid. Though the onset potential of Cu-$CuFe_2O_4$/C is inferior to Pt/C by 0.124 V, it clearly exceeds Pt/C in terms of the limiting current density by ~0.54 mA/cm^2. The increase in the limiting current density is essentially caused by the synergistic interaction of Vulcan carbon and Cu-$CuFe_2O_4$ NPs and increased mass transfer. Exposure to more active sites and seamless distribution of the Cu-$CuFe_2O_4$ NPs along with Vulcan carbon result in the improved limiting current density. Thus, the chemical mixing of Vulcan carbon with Cu-$CuFe_2O_4$ NPs simultaneously confirms better utilization of the active sites and superior synergistic interaction in the system, leading to the higher performance in ORR activity.

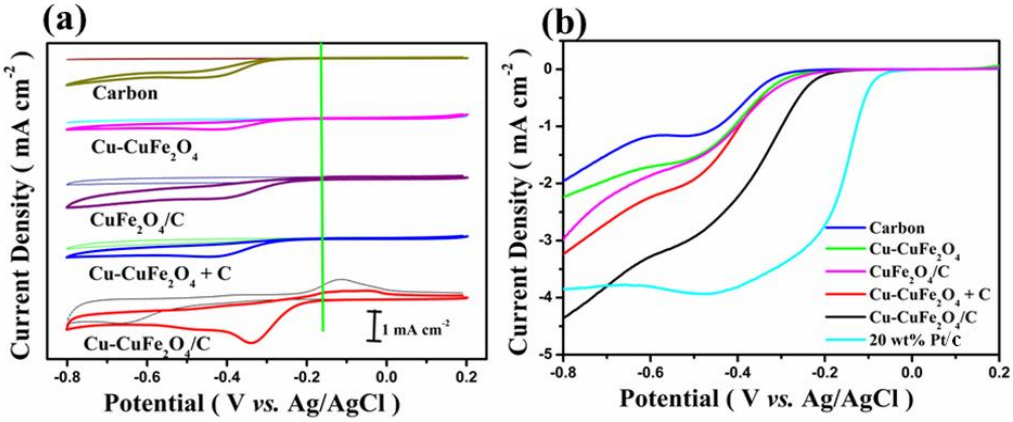

Figure 5A.6 (a) CVs of the Cu-$CuFe_2O_4$/C, Cu-$CuFe_2O_4$ + C mixture, Cu-$CuFe_2O_4$, and carbon on GCEs in an O_2-saturated (solid line) or N_2-saturated (dashed line) 0.1 M KOH solutions and (b) LSVs of the Cu-$CuFe_2O_4$/C, Cu-$CuFe_2O_4$ + C, Cu-$CuFe_2O_4$, carbon, and Pt/C in an O_2-saturated 0.1 M KOH solution at 1600 rpm.

The LSVs, K-L plots and "n" values of Cu-$CuFe_2O_4$/C and other electrocatalysts at various rotation rates are presented in Figure 5A.7-10. Figure 5A.7a presents the LSVs over Cu-$CuFe_2O_4$/C at different rotation rates between 400-3600 rpm in O_2-saturated 0.1 M KOH. Figure 5A.7b clearly shows good linear relationship and parallelism in the K−L plots derived from polarization curves at different potentials from −0.40 to −0.70 V. This indicates first-order kinetics of ORR w.r.t. oxygen concentration during the ORR process in selected potential range [24]. The "n" values calculated from the slope of the K−L plots shows to be ~4 in the broad

potential range from −0.4 to −0.7 V which infer that ORR proceeds via $4e^-$ process as presented in Figure 5A.7c.

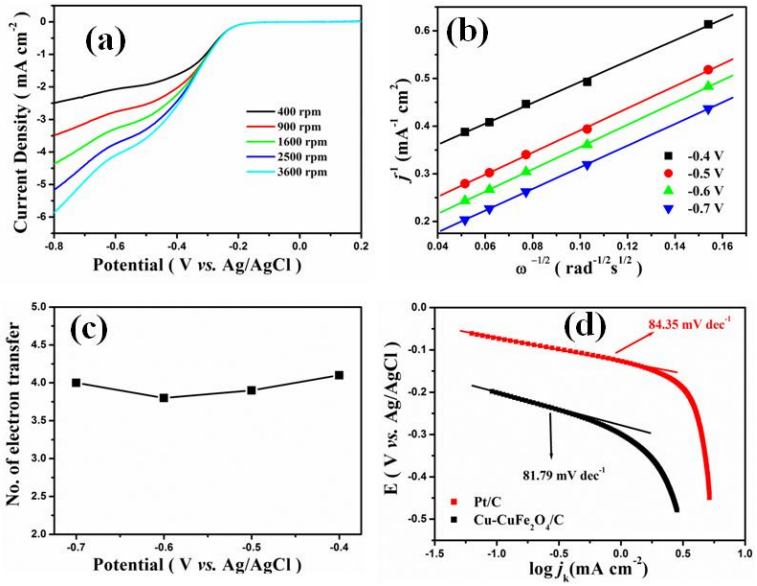

Figure 5A.7: (a) LSVs of the Cu-$CuFe_2O_4$/C NPs in O_2-saturated 0.1 M KOH solution at various rotation rates at a scan rate of 10 mV s^{-1}, (b) K−L plots in the potential range of −0.4 to −0.7 V, (c) the plot of the number of transferred electrons *vs.* potential for Cu-$CuFe_2O_4$/C NPs, (d) Tafel plots of Pt/C and Cu-$CuFe_2O_4$/C NPs.

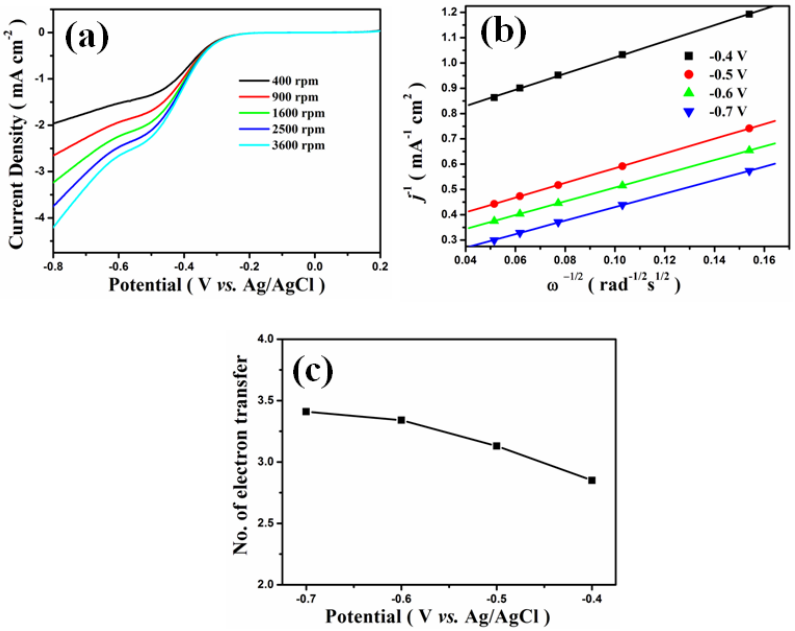

Figure 5A.8: (a) LSVs of the Cu-$CuFe_2O_4$ + C in O_2-saturated 0.1 M KOH solution at various rotation rates at a scan rate of 10 mV/s, (b) K−L plots in the potential range of −0.4 to −0.7 V, (c) the plot of number of transferred electrons *vs.* potential for Cu-$CuFe_2O_4$ + C.

To establish the importance of strong chemical interaction between Cu-$CuFe_2O_4$ and Carbon for improved ORR activity, we performed controlled experiments with physical mixture of Cu-$CuFe_2O_4$ and Carbon (Figure 5A.8), bare Cu-$CuFe_2O_4$ (Figure 5A.9) and $CuFe_2O_4$/C (Figure 5A.10). From the above discussion on Cu-$CuFe_2O_4$/C, Cu-$CuFe_2O_4$ + C and bare Cu-$CuFe_2O_4$ catalyzed ORR we can conclude that strong chemical interaction between Cu-$CuFe_2O_4$ and Carbon is indeed necessary for Cu-$CuFe_2O_4$ NPs to show the enhanced catalysis for the ORR.

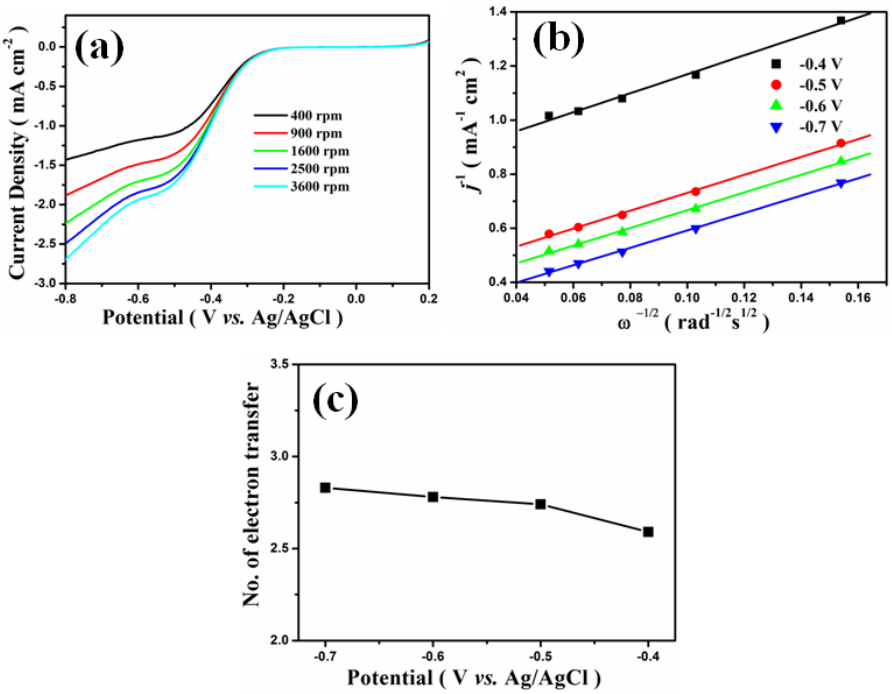

Figure 5A.9: (a) LSVs of the bare Cu-$CuFe_2O_4$ NPs in O2-saturated 0.1 M KOH solution at various rotation rates at a scan rate of 10 mV/s, (b) K−L plots in the potential range of −0.4 to −0.7 V, (c) the plot of number of transferred electrons vs. potential for bare Cu-$CuFe_2O_4$ NPs.

Chemical mixing with carbon and growth on carbon both make the Cu-$CuFe_2O_4$/C more conducting. Furthermore, growth on carbon matrix reduces the size of the Cu-$CuFe_2O_4$ NPs, (which were clearly visible in HR-TEM images) which could also contribute to the high ORR electrocatalytic activity in all respect.

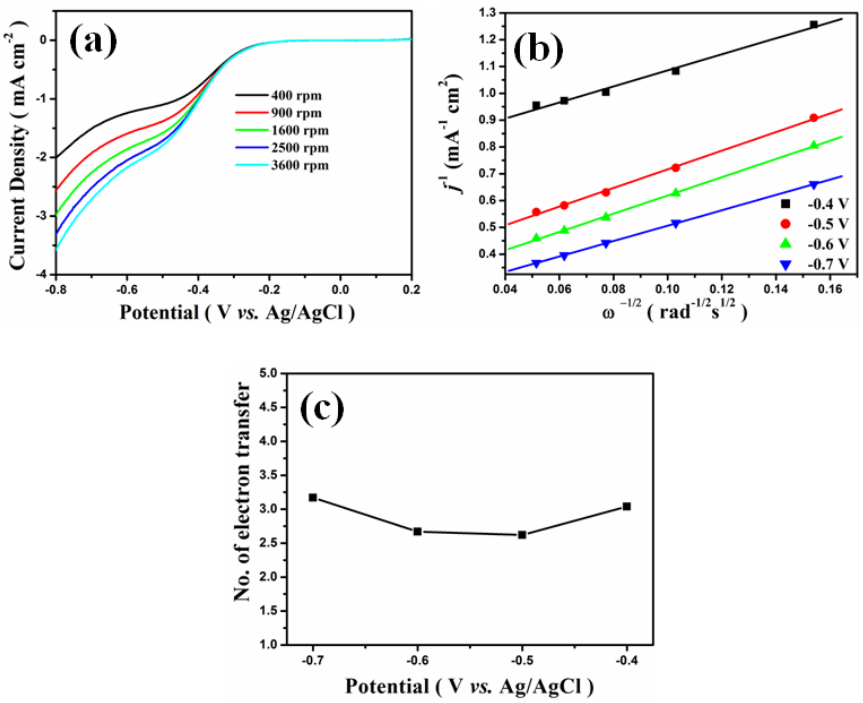

Figure 5A.10: (a) LSVs of the $CuFe_2O_4$/C NPs in O_2-saturated 0.1 M KOH solution at various rotation rates at a scan rate of 10 mV/s, (b) K−L plots in the potential range of −0.4 to −0.7 V, (c) the plot of number of transferred electrons *vs.* potential for $CuFe_2O_4$/C NPs.

More insightful information on the ORR kinetics gained from Tafel plots. Figure 5A.7d shows the comparative Tafel analysis for Cu-$CuFe_2O_4$/C and Pt/C. The relatively low Tafel slope of Cu-$CuFe_2O_4$/C (81.79 mV dec^{-1}) than Pt/C (84.35 mv dec^{-1}) signifies the ORR process involved faster kinetics. Furthermore, ECSA of the catalyst infer about the electrochemically active sites and reaction kinetics of the catalyst systems. The ECSA was calculated from the electrochemical double-layer capacitance (C_{dl}) using CV and presented in Figure 5A.11 [25]. A plot between double layer charging current *vs.* scan rates gives a straight line whose slope is equal to C_{dl}. High ECSA is the essential parameter for an effective electrocatalyst. The slope for the charging current of Cu-$CuFe_2O_4$/C is considerably higher than $CuFe_2O_4$/C., These results also show that the high catalytic activity of Cu-$CuFe_2O_4$/C can be credited to the enhanced conductivity resulting larger catalytically expose sites.

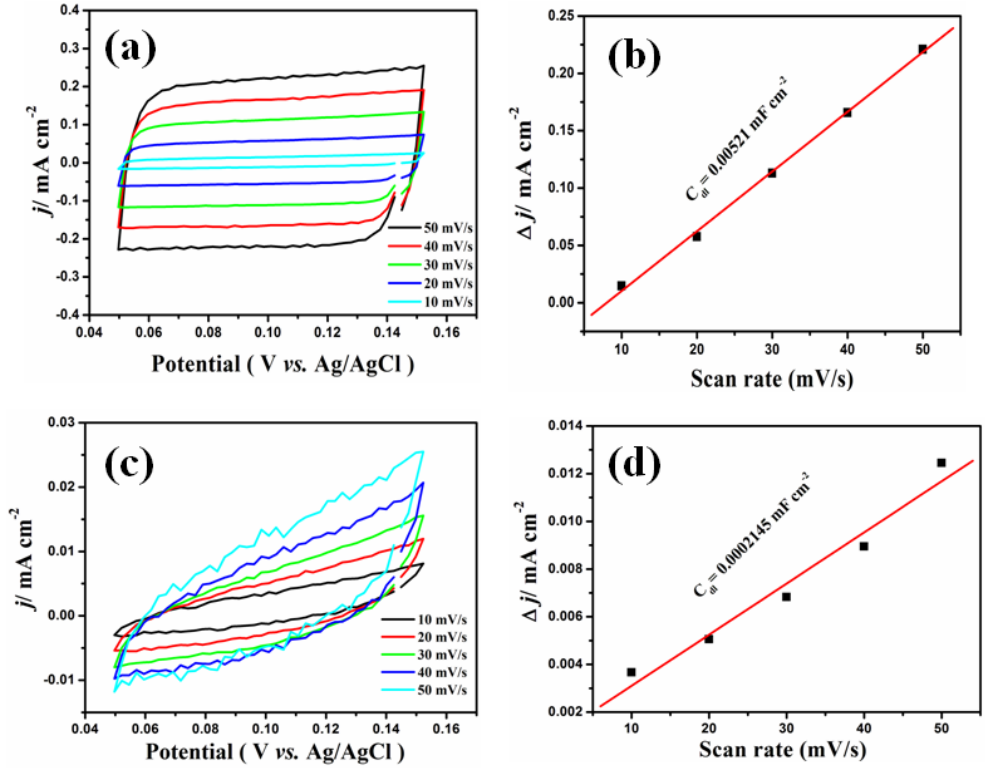

Figure 5A.11: CV curves of a) Cu-$CuFe_2O_4$/C and c) $CuFe_2O_4$/C NPs with different scan rates, charging current density differences as function of scan rates for b) Cu-$CuFe_2O_4$/C and d) $CuFe_2O_4$/C.

The mechanical and electrochemical stability of Cu-$CuFe_2O_4$/C in comparison to 20 wt % Pt/C has been examined by ADT, which involves measurement of the LSVs before and after subjecting the material under potential-induced conditions in the O_2-saturated electrolyte. The potential cycle was performed between −0.8 and 0.2 V (*vs.* Ag/AgCl) for 1000 cycles. Cu-$CuFe_2O_4$/C suffered 10 mV increase in the onset potential compared to a relatively high 59 mV shift observed in the case of Pt/C (Figure 5A.12a and 12b). However, the shift in the half-wave potential is found to be 20 mV in case of Cu-$CuFe_2O_4$/C and 26 mV for Pt/C. The better stability in terms of the onset and half-wave potential for Cu-$CuFe_2O_4$/C in comparison to Pt/C could be credited to the strong interaction of the Cu-$CuFe_2O_4$ NPs to carbon matrix.

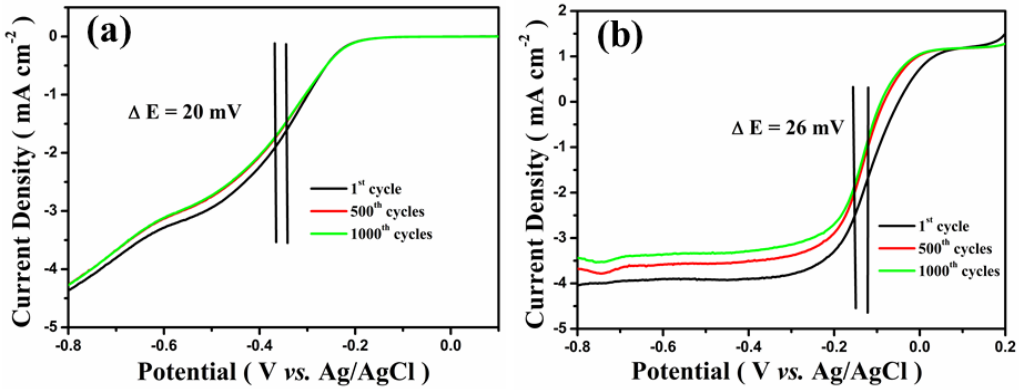

Figure 5A.12: ORR polarization curves of (a) Cu-$CuFe_2O_4$/C and (b) 20 wt% Pt/C at 1600 rpm in 0.1 M KOH solution before and after the stability test of different potential scans.

The electrochemical stability of the NPs was also assessed by the CA analysis in O_2-saturated 0.1 M KOH solutions at −0.3 V (*vs.* Ag/AgCl) and presented in Figure 5A.13. Cu-$CuFe_2O_4$/C has shown higher stability within 7200 sec over 20 wt % Pt/C. Cu-$CuFe_2O_4$/C maintained 80.5% of its initial current density, whereas Pt/C electrode retained 74.5% under the same experimental conditions.

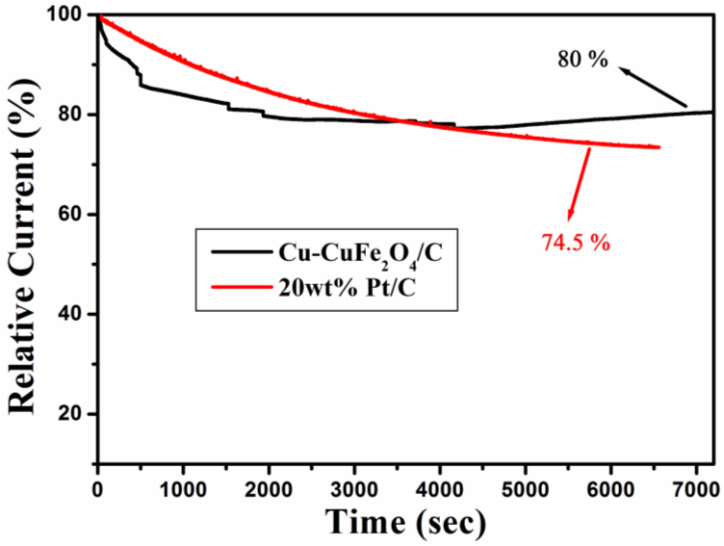

Figure 5A.13: CA curves of different NPs recorded at −0.3 V in O_2-saturated 0.1 M KOH solution with a rotation rate of 1600 rpm.

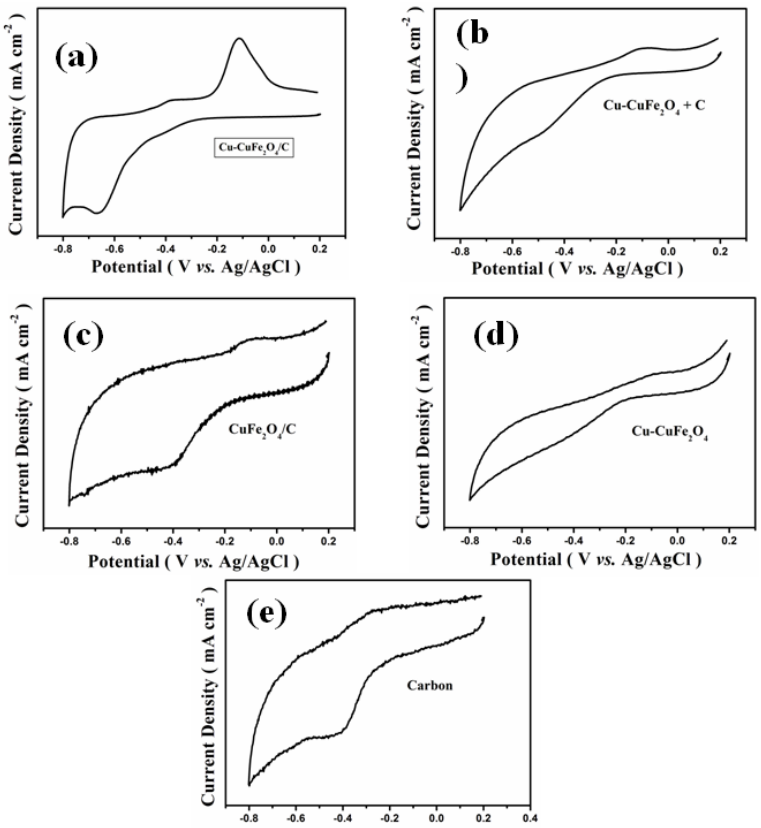

Figure 5A.14: CV curves of different catalysts recorded in N_2-saturated 0.1 M KOH solution.

Generally, the improved electrochemical performances of the Cu-$CuFe_2O_4$/C electrode can be endorsed to the synergistic effects among metallic Cu, $CuFe_2O_4$ particles, and carbon matrix, originated from the specific electrode configuration. The incorporated carbon matrix can offer nucleation sites for smaller crystal growth of Cu-$CuFe_2O_4$ without any agglomeration. The small size ensures the sufficient activation of active materials during reactions, resulting in the improvement of activity. Up to some limited extent, the magnetic behaviour of the copper ferrite catalyst plays an important role in showing better ORR performance according to previous report [11,26]. The highly conductive copper NPs anchored on carbon matrix provide more electrochemical reaction sites and also act as a conductive additive that assists the fast electronic transmission, which can lead to better limiting current density as well as

cycling stability. The advantages mentioned above result in the significant ORR performance of Cu-$CuFe_2O_4$/C.

To understand why the Cu-$CuFe_2O_4$/C NPs have such high activity, we studied the redox properties of all the studied catalysts in N_2-saturated 0.1 M KOH. Figure 5A.14 shows the typical CVs of the catalysts. We can see that all the catalysts (except carbon) exhibit an anodic redox peak in the range of −0.14 to −0.028 V (*vs*. Ag/AgCl) which is due to the Cu(I)/Cu(II) redox couple. Gurusamy et al. experimentally confirmed that the Cu(I)/Cu(II) redox couple is very essential for the catalyzing the ORR [27] as Cu(I)/Cu(II) helps as the redox mediator throughout ORR. The Cu (I)/Cu(II) redox mediator may transmit electron from the electrode to the catalyst sites and quicken the reduction of oxygen [28]. In this case, the Cu(I)/Cu(II) redox couple is more prominent in case of Cu-$CuFe_2O_4$/C among all catalysts. This may explain why Cu-$CuFe_2O_4$/C NPs show superior ORR activity among all other catalysts.

5A.2 Conclusions

In summary, Cu-$CuFe_2O_4$/C with superior ORR property has been successfully synthesized by a facile one-step solvothermal approach. The well-defined Cu-$CuFe_2O_4$ NPs are uniformly dispersed on the carbon matrix. The integration of Cu with $CuFe_2O_4$ NPs along with the chemical interaction with the carbon matrix can accelerate the transportation of electrons/ion resulting in the enhancement of ORR performance by increasing the structural and interfacial stability. The Cu-$CuFe_2O_4$/C shows a high limiting current density Cu-$CuFe_2O_4$ + C, bare Cu-$CuFe_2O_4$ and Vulcan carbon. In particular, Cu-$CuFe_2O_4$/C can deliver high limiting current density (0.54 mA/cm^2) and electrochemical stability than state of the art 20 wt% Pt/C. Such outstanding electrochemical performances make the copper ferrites as promising materials for the energy-related devices.

Section 5B: Synthesis and Characterization of CuCo/CuO-Co_3O_4/C Nanoparticles and Their Electrochemical Oxygen Reduction Reaction Activity

In the section 5B, CuCo/CuO-Co_3O_4/C NPs were synthesized via solvothermal method and characterized by various spectroscopic and analytical techniques. The electrocatalytic activities of the synthesized NPs were evaluated for ORR in alkaline media.

5B.1 Results and Discussion

5B.1.1 Characterization of the Ssynthesized CuCo/CuO-Co_3O_4/C NPs

XRD pattern of CuCo/CuO-Co_3O_4/C NPs clearly indicates the formation of interfacial bimetallic fused cluster along with mixed CuO-Co_3O_4 as shown in Figure 5B.1. The diffraction peaks with 2θ = 43.3°, 50.4° and 74.0° can be indexed to (111), (200) and (220) reflection of fcc Cu (JCPDS No. 85-1326) and 44.4°, 51.3°, and 75.5° to (111), (200) and (220) of fcc Co (JCPDS No. 89-4307). CuO and Co_3O_4 diffraction peaks are indexed to JCPDS No. 80-1268 and 65-3103, respectively. In case of CuO-Co_3O_4/C, there is no diffraction peaks observed for the metallic Cu and Co.

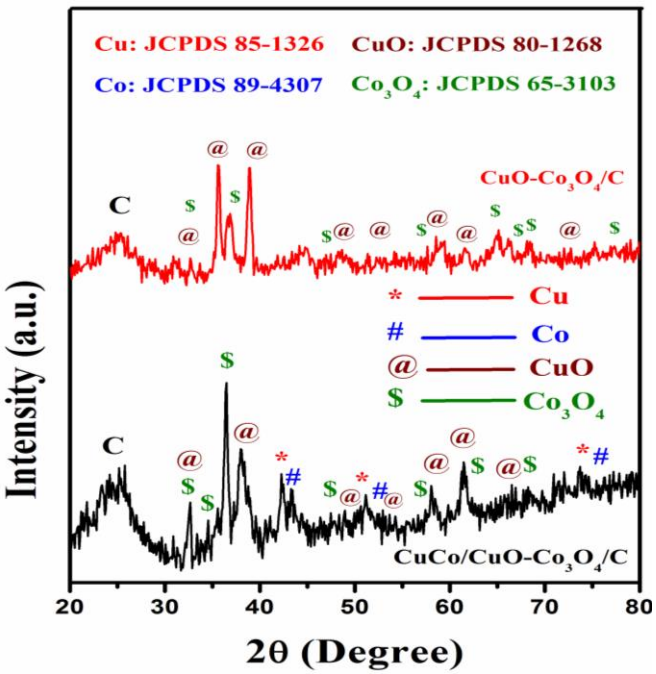

Figure 5B.1: XRD patterns of CuCo/CuO-Co_3O_4/C and CuO-Co_3O_4/C NPs.

Figure 5B.2 represents the TGA profile of CuCo/CuO-Co_3O_4/C NPs at air atmosphere. From TGA drastic change of weight is observed between 350 and 500 °C, which is due to the burning of the carbonaceous materials under air atmosphere. After burning all the carbonaceous material, the residue remains ~25 % corresponding to CuCo/CuO-Co_3O_4.

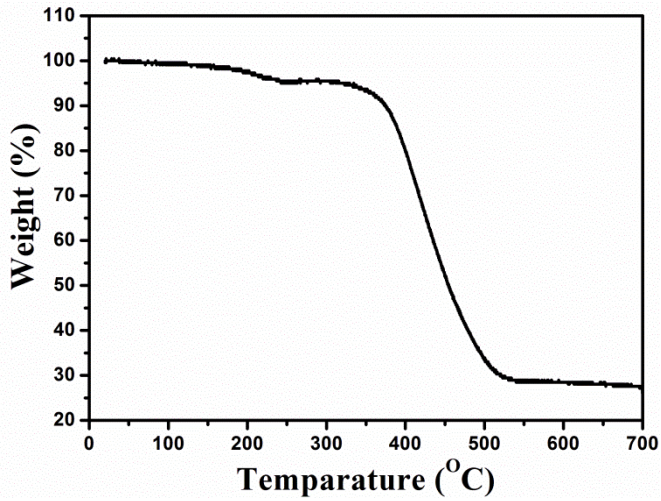

Figure 5B.2: TGA curve of CuCo/CuO-Co_3O_4/C in air atmosphere.

N_2 adsorption/desorption experiments was performed to investigate the surface and textural property of CuCo/CuO-Co_3O_4/C NPs and presented in Figure 5B.3. It was found that the BET surface area of CuCo/CuO-Co_3O_4/C is 160.7 m^2/g and BJH pore diameter is 15.7 Å.

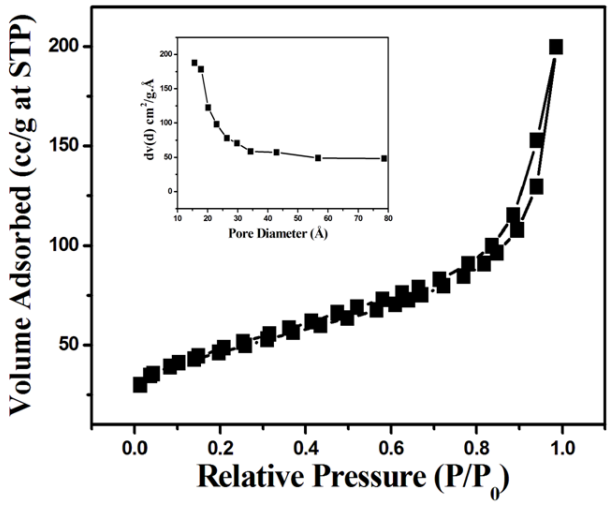

Figure 5B.3: N_2 adsorption/desorption isotherm and the pore size distribution curve (inset) of CuCo/CuO-Co_3O_4/C NPs.

TEM images (Figure 5B.4) are recorded to investigate the size and morphology of the synthesized CuCo/CuO-Co_3O_4/C NPs. From the TEM images the morphology of the NPs was found to be spherical with particle size below 20 nm.

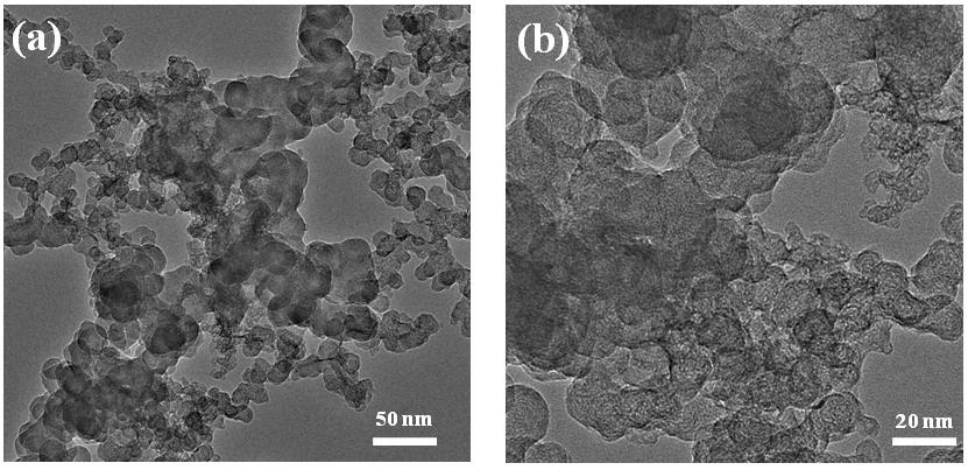

Figure 5B.4: (a),(b) TEM images of CuCo/CuO-Co_3O_4/C NPs at different resolution.

XPS was used to analyze the composition and oxidation state of Cu and Co in CuCo/CuO-Co_3O_4/C NPs. The survey scan XP spectrum of the NPs indicates the existence of Cu 2p, Co 2p, O 1s and C 1s (Figure 5B.5a). Figure 5B.5b represents the C 1s spectra of the samples, due to the asymmetric nature it could be deconvoluted into three peaks at 284.6 (-C=C-), 286.1 (-C-O-) and 290 eV (O=C-O-). As shown in Figure 5B.5c, the core-level Cu 2p spectra of CuCo/CuO-Co_3O_4/C NPs display signal with binding energies of 932.5 and 952.87 eV for Cu $2p_{3/2}$ and Cu $2p_{1/2}$ corresponding to Cu^0 NPs. Additional peaks with binding energies at 934.1 and 954.2 eV is due to the presence of Cu^{2+}. The two other peaks centered at 941.2 (Cu $2p_{3/2}$) and 961.3 (Cu $2p_{1/2}$) eV are satellites peaks for Cu 2p spectra [29,30]. Also, the detailed core-level spectrum of the Co 2p is presented in Figure 5B.5d. Core-level spectrum of Co 2p is presented in Figure 5B.5d. In this spectrum, Co $2p_{3/2}$ and Co $2p_{1/2}$ peaks are deconvoluted into six peaks with binding energy 778.4, 780.19 and 782.3 eV and 793.9, 795.34 and 797.86 eV, assigned to Co^o, Co^{2+} and Co^{3+} respectively [31].

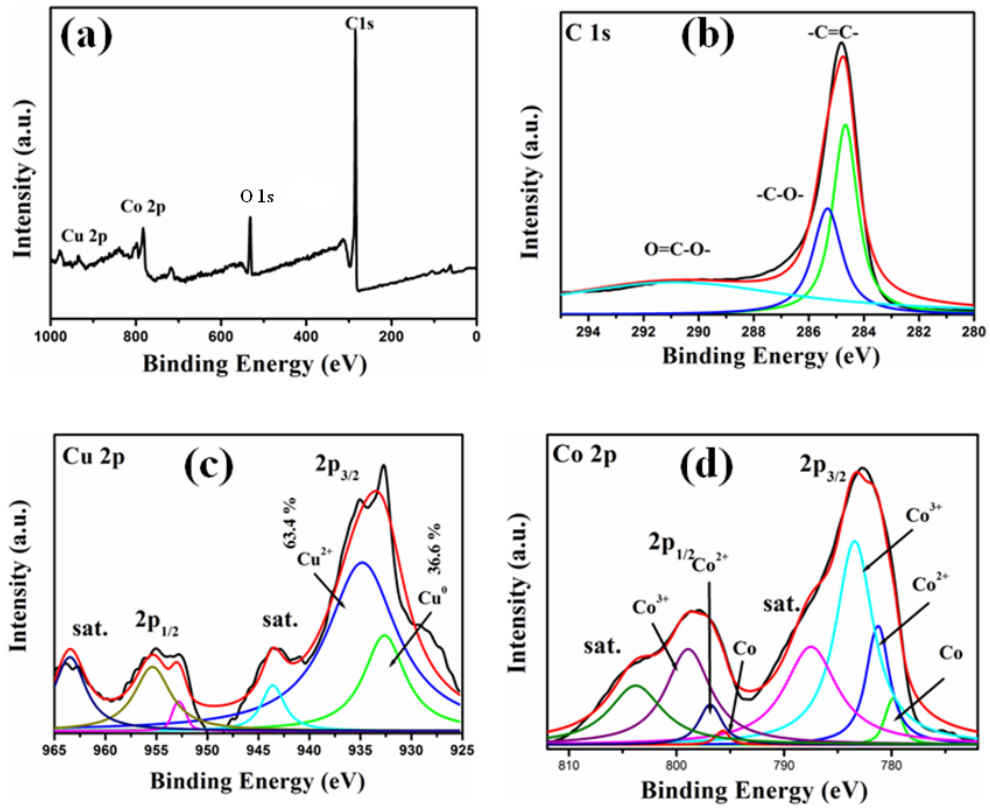

Figure 5B.5: XPS analysis for CuCo/CuO-Co_3O_4/C NPs (a) the survey spectrum; and the high resolution core-level XP-spectrum of (b) C 1s, (c) Cu 2p and (d) Co 2p region.

5B.1.2 Electrocatalytic Activity of CuCo/CuO-Co_3O_4/C NPs

The electrocatalytic activities towards ORR of CuCo/CuO-Co_3O_4/C and other NPs were studied by CV and RDE measurements. The CV plots of Co/C, Cu/C, CuO-Co_3O_4/C, CuCo/CuO-Co_3O_4 + C, CuCo/CuO-Co_3O_4/C and CuCo/CuO-Co_3O_4 NPs in both N_2- and O_2-saturated environment 0.1 M KOH solution are shown in Figure 5B.6, respectively. The CV plots clearly indicate that all electrocatalysts exhibit a strong cathodic peak with high current density at O_2-saturated 0.1 M KOH solution compared to N_2-saturated solution. This infers that the all NPs are active ORR.

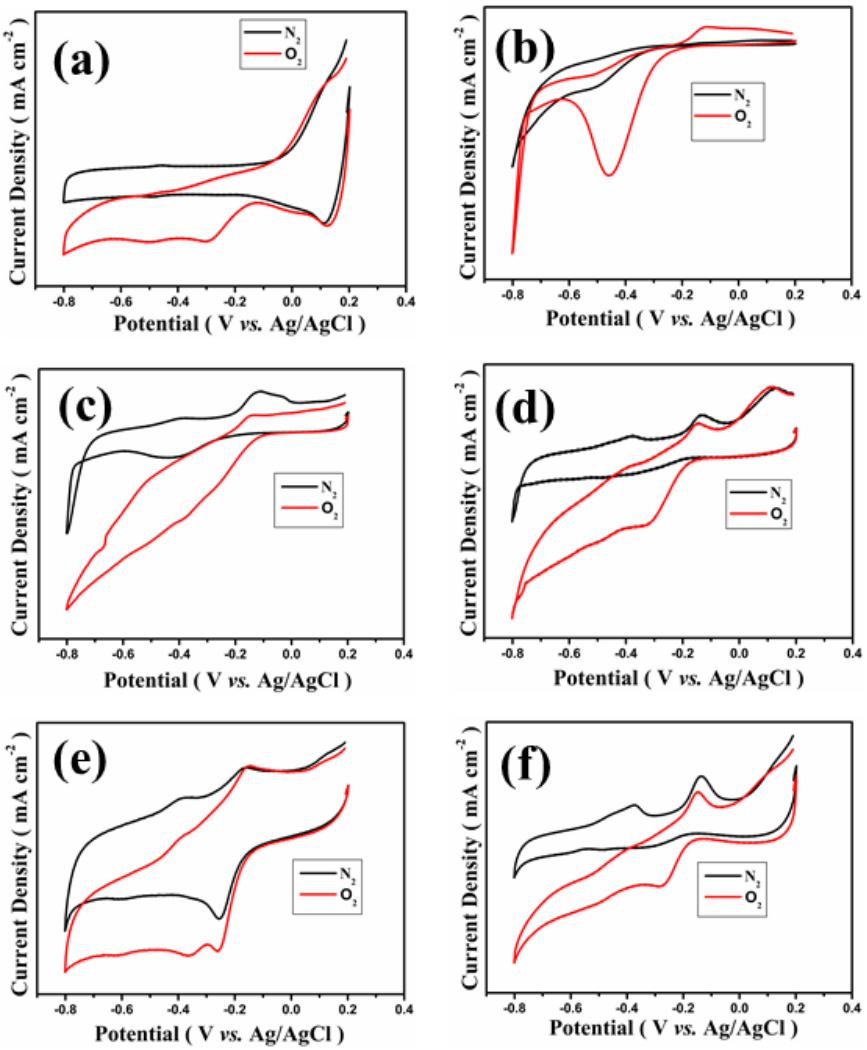

Figure 5B.6: CV plots of (a) Co/C, (b) Cu/C, (c) CuO-Co_3O_4/C, (d) CuCo/CuO-Co_3O_4 + C, (e) CuCo/CuO-Co_3O_4/C and (f) CuCo/CuO-Co_3O_4 NPs in both N_2- and O_2-saturated 0.1 M KOH solution.

The ORR activity for all the electrocatalysts was further investigated by RDE/LSV measurements at the rotating speeds of 400, 900, 1600, 2500 and 3600 rpm. The representative LSVs for Co/C, Cu/C, CuO-Co_3O_4/C, CuCo/CuO-Co_3O_4+C, CuCo/CuO-Co_3O_4/C and CuCo/CuO-Co_3O_4 are shown in the Figure 5B.7(a-f), respectively.

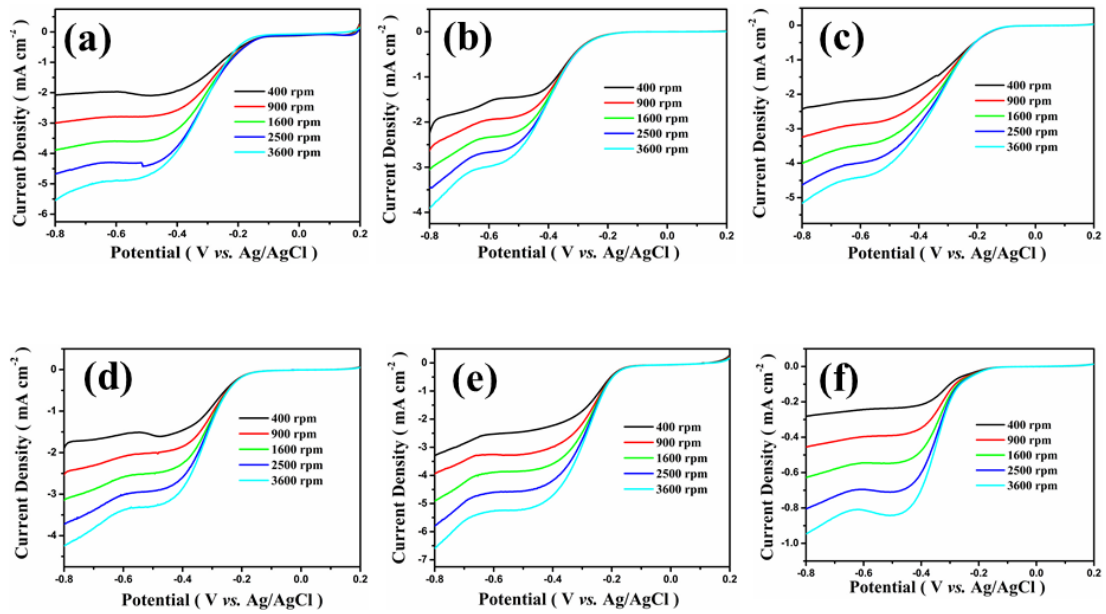

Figure 5B.7: Rotating rate dependent LSVs at the scan rate of 10 mV s^{-1} in O_2-saturated 0.1 M KOH over (a) Co/C, (b) Cu/C, (c) CuO-Co_3O_4/C, (d) CuCo/CuO-Co_3O_4 + C, (e) CuCo/CuO-Co_3O_4/C and (f) CuCo/CuO-Co_3O_4, respectively.

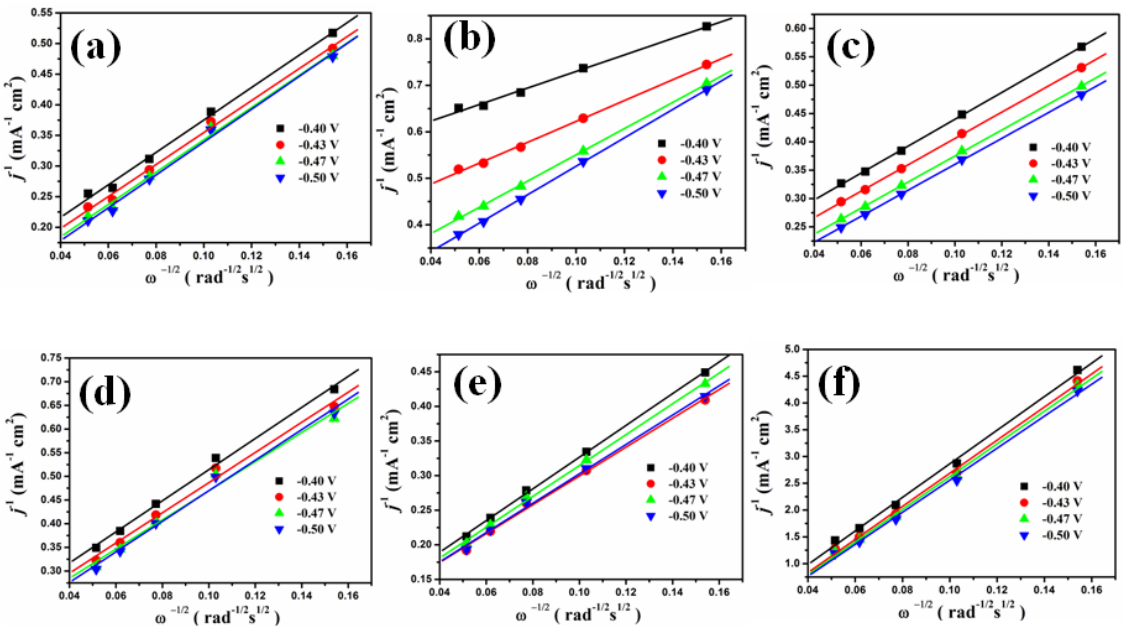

Figure 5B.8: K-L plots at different potentials for (a) Co/C, (b) Cu/C, (c) CuO-Co_3O_4/C, (d) CuCo/CuO-Co_3O_4+ C, (e) CuCo/CuO-Co_3O_4/C and (f) CuCo/CuO-Co_3O_4, respectively.

Figure 5B.8 represents the K-L plots of (a) Co/C, (b) Cu/C, (c) CuO-Co_3O_4/C, (d) CuCo/CuO-Co_3O_4+C, (e) CuCo/CuO-Co_3O_4/C and (f) CuCo/CuO-Co_3O_4, respectively. The K-L plots in the potential range –0.40 to –0.50 V displays good linearity for all the electrocatalysts. From the plots it can be predicted that all the NPs follows first order ORR kinetics. The "n" in ORR is calculated from the slope of K-L plots as mentioned in Chapter 2. The "n" values are found to be ~4 in case of Co/C, Cu/C, CuO-Co_3O_4/C and CuCo/CuO-Co_3O_4/C, but ~2 for CuCo/CuO-Co_3O_4+C and CuCo/CuO-Co_3O_4. These results conclude that Co/C, Cu/C, CuO-Co_3O_4/C and CuCo/CuO-Co_3O_4/C proceed via $4e^-$ pathway in the ORR process. To compare the ORR activity of all the catalysts with commercial 20 wt% Pt/C, we have compared their LSVs at 1600 rpm as presented in Figure 5B.9. From the above discussion, it is clearly seen that Cu/C and Co/C have inferior ORR activity than the CuCo/CuO-Co_3O_4/C, which may be due to the synergistic interaction. Moreover, the strong chemical interaction between NPs and Vulcan carbon is a key factor for the improved ORR activity. For this, we performed control experiments by physically mixing CuCo/CuO-Co_3O_4 and Carbon through sonication (mixture 20 wt%, Figure 5B.7d) and bare CuCo/CuO-Co_3O_4 (Figure 5B.7f). From the above discussion, we notice that CuCo/CuO-Co_3O_4 + C and bare CuCo/CuO-Co_3O_4 NPs shows inferior activity in all respect (onset potential, half-wave potential, current density, and "n" values) during ORR process than CuCo/CuO-Co_3O_4/C. In another experiment, CuO-Co_3O_4/C also shows inferior activity in all respect (onset potential, half-wave potential and current density) than CuCo/CuO-Co_3O_4/C. Thus the presence of metal and metal oxides interfaces makes CuCo/CuO-Co_3O_4/C more conductive and eventually tender improved ORR activity.

For more insightful information on the ORR kinetics, Tafel plots are depicted in Figure 5B.10 for CuCo/CuO-Co_3O_4/C and Pt/C. The relatively low Tafel slope of CuCo/CuO-Co_3O_4/C (75.96 mV dec^{-1}) than that of Pt/C (84.35 mv dec^{-1}) implies that ORR process involved faster kinetics. Furthermore, ECSA of the catalyst provides the information of electrochemically active sites and reaction kinetics of electrocatalyst.

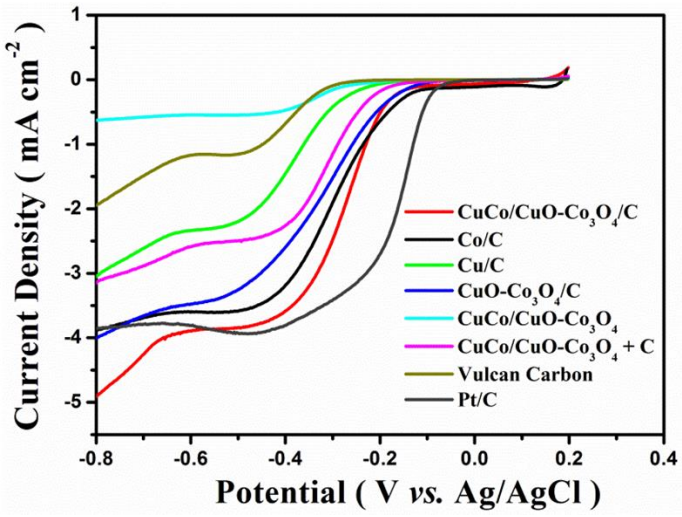

Figure 5B.9: LSVs of the all electrocatalysts in O_2-saturated 0.1 M KOH solution at 1600 rpm.

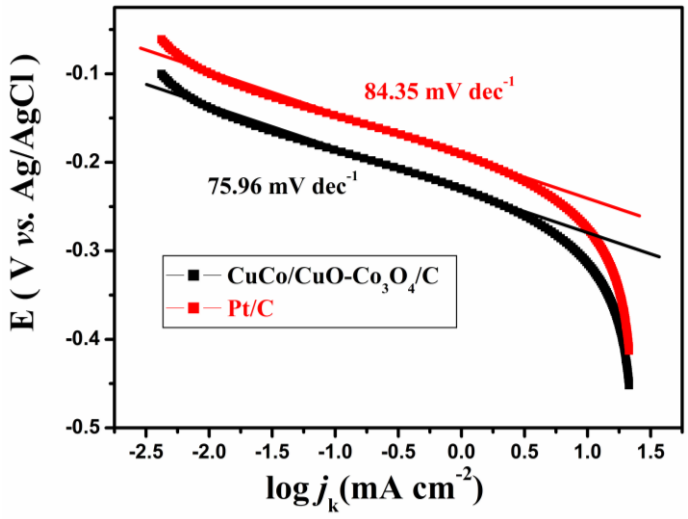

Figure 5B.10: The Tafel plots of Pt/C and CuCo/CuO-Co_3O_4/C NPs.

The ECSA of the catalyst is estimated from C_{dl} using CV [25]. A plot between double layer charging current *vs.* scan rates gives a straight line whose slope is equal to C_{dl}. High ECSA is the essential parameter for an effective catalyst system. The slope for the charging current of CuCo/CuO-Co_3O_4/C is considerably higher than CuO-Co_3O_4/C, which specifies large electrochemically active sites available on the surface for superior ORR activity. These results also show that the high catalytic activity of CuCo/CuO-Co_3O_4/C can be credited to the enhanced conductivity resulting larger catalytically exposed sites (Figure 5B.11).

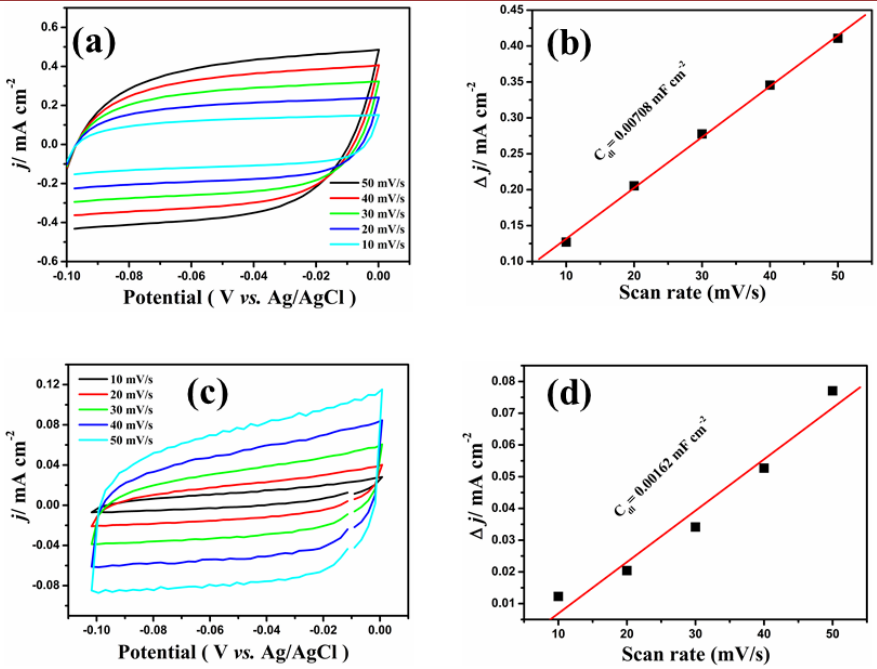

Figure 5B.11: CV curves of a) CuCo/CuO-Co_3O_4/C and c) CuCo/CuO-Co_3O_4 NPs with different scan rates. (D) Charging current density differences as function of scan rates for b) CuCo/CuO-Co_3O_4/C and d) CuCo/CuO-Co_3O_4.

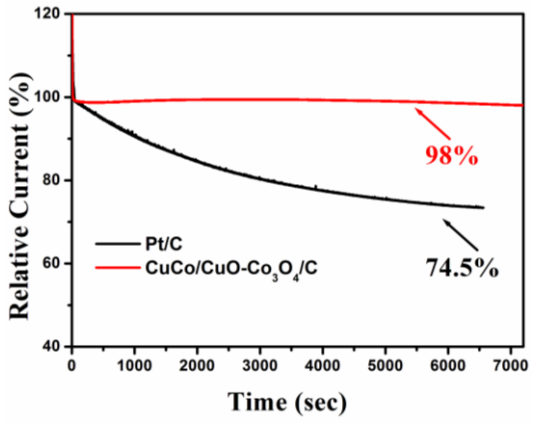

Figure 5B.12: CA curves of different catalysts, recorded at −0.3 V in O_2-saturated 0.1 M KOH solution with a rotation rate of 1600 rpm.

For the practical application of electrocatalyst, stability is the important parameter. The electrochemical stability of the catalysts was evaluated by the CA test in O_2-saturated 0.1 M KOH solutions at −0.3 V (*vs.* Ag/AgCl). As shown in Figure 5B.12, CuCo/CuO-Co_3O_4/C has shown higher stability within 7200 sec. The CuCo/CuO-Co_3O_4/C retained 98% of its initial current density, whereas Pt/C retained 74.5% under the same experimental conditions. Usually, the enhanced electrochemical

property of the CuCo/CuO-Co_3O_4/C electrode can be originated from the synergistic effects among metallic Cu, and Co, and the chemical interaction between the NPs and carbon matrix. This provided specific electrode configuration, the incorporated carbon matrix can offer nucleation sites for smaller crystal growth without any agglomeration. Moreover, the highly conductive Cu and Co NPs attached on carbon matrix provide more electrochemical reaction sites and also act as conductive additives that assist fast electron flow leading to the higher limiting current density as well as stability towards ORR.

5B.2 Conclusions

In conclusion, CuCo/CuO-Co_3O_4/C NPs were synthesized by facile one-step solvothermal method using hydrazine hydrate as reducing agent. The NPs showed very efficient electrocatalytic activity toward ORR in alkaline media. It shows high limiting current density than Cu/C, Co/C, CuCo/CuO-Co_3O_4 + C, CuCo/CuO-Co_3O_4, and Vulcan carbon. From these observations it is easily understood that synergistic interaction, chemical interaction between the NPs and carbon are essential parameters for the improved ORR activity. Moreover, the integration of Cu and Co to CuO-Co_3O_4 along with the chemical interaction with the carbon matrix can accelerate the transportation of electrons/ion resulting in the enhancement of ORR performance by increasing the structural and interfacial stability. Thus, the present investigation provides a remarkable application of CuCo/CuO-Co_3O_4/C NPs in the fields of fuel cell ORR in alkaline media.

References

[1] Mehta, V., and Cooper, J. S. Review and analysis of PEM fuel cell design and manufacturing. *Journal of Power Sources*, 114(1):32−53, 2003.

[2] Li, Y., and Dai, H. Recent advances in zinc–air batteries. *Chem. Soc. Rev.*, *Chemical Society Reviews*, 43(15):5257−5275, 2014.

[3] Wang, G., Zhang, L., and Zhang, J. A review of electrode materials for electrochemical supercapacitors. *Chemical Society Reviews*, 41(2):797 − 828, 2012.

[4] Wang, J., Deng, Q., Li, M., Jiang, K., Zhang, J., Hu, Z., and Chu, J. Copper ferrites@reduced graphene oxide anode materials for advanced lithium storage applications. *Scientific Reports*, 7(1):8903, 2017.

[5] Nie, Y., Li, L., and Wei, Z. Recent advancements in Pt and Pt-free catalysts for oxygen reduction reaction. *Chemical Society Reviews*, 44(8):2168−2201, 2015.

[6] Zhang, Z., More, K. L., Sun, K., Wu, Z., and Li, W. Preparation and characterization of PdFe nanoleaves as electrocatalysts for oxygen reduction reaction. *Chemistry of Materials*, 23(6):1570−1577, 2011.

[7] Yan, X., Jia, Y., Zhang, L., Teng Soo, M., and Yao, X. Defective graphene anchored iron–cobalt nanoparticles for efficient electrocatalytic oxygen reduction. *Chemical Communications*, 53(89):12140−12143, 2017.

[8] Tritsaris, G. A., Nørskov, J. K., and Rossmeisl, J. Trends in oxygen reduction and methanol activation on transition metal chalcogenides. *Electrochimica Acta*, 56(27):9783−9788, 2011.

[9] Cao, B., Veith, G. M., Diaz, R. E., Liu, J., Stach, E. A., Adzic, R. R., and Khalifah, P. G. Cobalt molybdenum oxynitrides: synthesis, structural characterization, and catalytic activity for the oxygen reduction reaction. *Angewandte Chemie International Edition*, 52(41):10753−10757, 2013.

[10] Toh, R. J., Eng, A. Y. S., Sofer, Z., Sedmidubsky, D., and Pumera, M. Ternary transition metal oxide nanoparticles with spinel structure for the oxygen reduction reaction. *ChemElectroChem*, 2(7):982−987, 2015.

[11] Zhu, H., Zhang, S., Huang, Y.-X., Wu, L., and Sun, S. Monodisperse $M_xFe_{3-x}O_4$ (M = Fe, Cu, Co, Mn) nanoparticles and their electrocatalysis for oxygen reduction reaction. *Nano Letters*, 13(6):2947−2951, 2013.

[12] Kashyap, V., Singh, S. K., and Kurungot, S. Cobalt ferrite bearing nitrogen-doped reduced graphene oxide layers spatially separated with microporous carbon as efficient oxygen reduction electrocatalyst. *ACS Applied Materials and Interfaces*, 8(32):20730−20740, 2016.

[13] Ning, R., Tian, J., Asiri, A. M., Qusti, A. H., Al-Youbi, A. O., and Sun, X. Spinel $CuCo_2O_4$ nanoparticles supported on N-doped reduced graphene oxide: A highly active and stable hybrid electrocatalyst for the oxygen reduction reaction. *Langmuir*, 29(43):13146−13151, 2013.

[14] Singh, S. K., Kashyap, V., Manna, N., Bhange, S. N., Soni, R., Boukherroub, R., Szunerits, S., and Kurungot, S. Efficient and durable oxygen reduction electrocatalyst based on CoMn alloy oxide nanoparticles supported over N-doped porous graphene. *ACS Catalysis*, 7(10):6700−6710, 2017.

[15] Zhao, S.-Y., Zhang, B., Su, H., Zhang, J.-J., Li, X.-H., Wang, K.-X., Chen, J.-S., Wei, X., and Feng, P. Enhanced oxygen electroreduction over nitrogen-free carbon nanotube-supported $CuFeO_2$ nanoparticles. *Journal of Materials Chemistry A*, 6(10):4331−4336, 2018.

[16] Wang, M., Su, C., Saunders, M., Liang, J., Shao, Z., Wang, S., and Liu, J. Yolk-shell-structured Cu/Fe@γ-Fe_2O_3 nanoparticles loaded graphitic porous carbon for the oxygen reduction reaction. *Particle & Particle Systems Characterization*, 34(10):1700158, 2017.

[17] Dong, Y., Chui, Y.-S., Ma, R., Cao, C., Cheng, H., Li, Y. Y., and Zapien, J. A. One-pot scalable synthesis of Cu–$CuFe_2O_4$/graphene composites as anode materials for lithium-ion batteries with enhanced lithium storage properties. *Journal of Materials Chemistry A*, 2(34):13892−13897, 2014.

[18] Xing, G. Z., Yi, J. B., Tao, J. G., Liu, T., Wong, L. M., Zhang, Z., Li, G. P., Wang, S. J., Ding, J., Sum, T. C., Huan, C. H. A., and Wu, T. Comparative study of room-temperature ferromagnetism in Cu-Doped ZnO nanowires enhanced by structural inhomogeneity. *Advanced Materials*, 20(18):3521−3527, 2008.

[19] Lu, Y., Zhao, S., Yang, R., Xu, D., Yang, J., Lin, Y., Shi, N.-E., Dai, Z., Bao, J., and Han, M. Well-coupled nanohybrids obtained by component-controlled synthesis and in situ integration of Mn_xPd_y nanocrystals on vulcan carbon for electrocatalytic oxygen reduction. *ACS Applied Materials & Interfaces*, 10(9):8155−8164, 2018.

[20] Sun, C., Rajasekhara, S., Goodenough, J. B., and Zhou, F. Monodisperse porous $LiFePO_4$ microspheres for a high power Li-ion battery cathode. *Journal of the American Chemical Society*, 133(7):2132−2135, 2011.

[21] Liang, Y., Li, Y., Wang, H., Zhou, J., Wang, J., Regier, T., and Dai, H. Co_3O_4 nanocrystals on graphene as a synergistic catalyst for oxygen reduction reaction. *Nature Materials*, 10(10):780−786, 2011.

[22] Mao, S., Wen, Z., Huang, T., Hou, Y., and Chen, J. High-performance bi-functional electrocatalysts of 3D crumpled graphene–cobalt oxide nanohybrids for oxygen reduction and evolution reactions. *Energy & Environmental Science.*, 7(2):609−616, 2014.

[23] Liang, Y., Li, Y., Wang, H., and Dai, H. Strongly coupled inorganic/nanocarbon hybrid materials for advanced electrocatalysis. *Journal of the American Chemical Society*, 135(6):2013−2036, 2013.

[24] Jäger, R., Härk, E., Romann, T., Joost, U., and Lust, E. C(Mo_2C) and Pt–C (Mo_2C) based mixed catalysts for oxygen reduction reaction. *Journal of Electroanalytical Chemistry*, 761:89−97, 2016.

[25] Lukowski, M. A., Daniel, A. S., Meng, F., Forticaux, A., Li, L., and Jin, S. Enhanced hydrogen evolution catalysis from chemically exfoliated metallic MoS_2 nanosheets. *Journal of the American Chemical Society*, 135(28):10274−10277, 2013.

[26] Monzon, L. M. A., Rode, K., Venkatesan, M., and Coey, J. M. D. Electrosynthesis of iron, cobalt, and zinc microcrystals and magnetic enhancement of the oxygen reduction reaction. *Chemistry of Materials*, 24(20):3878−3885, 2012.

[27] Gurusamy, T., Gayathri, P., Mandal, S., and Ramanujam, K. Redox-active copper-benzotriazole stacked multiwalled carbon nanotubes for the oxygen reduction reaction. *ChemElectroChem*, 5(14):1837−1847, 2018.

[28] He, Q., Yang, X., Ren, X., Koel, B. E., Ramaswamy, N., Mukerjee, S., and Kostecki, R. A novel CuFe-based catalyst for the oxygen reduction reaction in alkaline media. *Journal of Power Sources*, 196(18):7404−7410, 2011.

[29] Dong, Y., Chui, Y.-S., Ma, R., Cao, C., Cheng, H., Li, Y. Y., and Zapien, J. A. One-pot scalable synthesis of Cu–$CuFe_2O_4$/graphene composites as anode materials for lithium-ion batteries with enhanced lithium storage properties. *Journal of Materials Chemistry A*, 2(34):13892, 2014.

[30] Xing, G. Z., Yi, J. B., Tao, J. G., Liu, T., Wong, L. M., Zhang, Z., Li, G. P., Wang, S. J., Ding, J., Sum, T. C., Huan, C. H. A., and Wu, T. Comparative study of room-temperature ferromagnetism in Cu-Doped ZnO nanowires enhanced by structural inhomogeneity. *Advanced Materials*, 20(18):3521−3527,

2008.

[31] Rezaee, S., and Shahrokhian, S. Facile synthesis of petal-like NiCo/NiO-CoO/nanoporous carbon composite based on mixed-metallic MOFs and their application for electrocatalytic oxidation of methanol. *Applied Catalysis B: Environmental*, 244:802−813, 2019.